RADIATIVE BALANCE OVER A ROUGH SNOW SURFACE - OBSERVATIONS AND MODELLING AT METER AND MOUNTAIN RANGE SCALES

MASTER THESIS

Inès OLLIVIER

Supervisors	Dr. Fanny LARUE & Prof. Ghislain PICARD	IGE
Reviewer	Res. Dir. Jean Pierre LAGOUARDE	INRA

Prepared at Institut des Géosciences de l'Environnement (IGE), Grenoble, France

M2 Sciences de la Terre et des Planètes, Environnement, parcours Atmosphère, Climat, Surfaces Continentales, Université Grenoble Alpes, France
Academic year 2018-2019

Master in Earth, planetary and Environmental Sciences
Non-plagiarism certificate

I, the undersigned *Inès OLLIVIER*
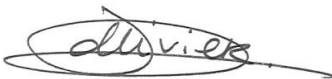
Author of the report entitled

Radiative balance over a rough snow surface – observations and modelling at meter and mountain range scales

Declare that the above-cited report results from my personal work and that I have neither forged, falsified nor copied all or part of another persons work to present it as mine.

All sources of information used and all author citations have been included following standard usage.

I am aware of the fact that failing to cite a source or failing to cite it fully and properly constitutes plagiarism, and that plagiarism is considered a serious offence within the university that can be sanctioned everely by law.

At St Martin d'Hères,
the 14/06/2019.

Résumé

Les surfaces enneigées sont généralement représentées dans les modèles de neige comme des surfaces plates et lisses. En réalité, la présence de rugosités à la surface de la neige peut introduire des biais dans les simulations de l'évolution du manteau neigeux. Ces rugosités peuvent être de différentes échelles, de l'échelle métrique (sastrugi, dunes de neige) à kilométrique (versants montagneux). En piégeant les photons entre leurs bords, les rugosités ont un impact majeur sur la température de surface de la neige, ainsi que sur le bilan radiatif de cette surface. Néanmoins, cet effet est peu connu et modélisé. Un modèle de ray-tracing appelé RSRT à été récemment développé à l'IGE pour simuler les interactions entre le rayonnement solaire et les surfaces rugueuses. Cette étude vise à 1) mesurer les variations temporelles et spatiales de la température de surface de la neige, et 2) développer une chaine de calculs pour estimer la température de la neige sur des surfaces rugueuses en utilisant les sorties du modèle RSRT. Trois campagnes de mesures de terrain ont été organisées pendant l'hiver 2019, dans des régions montagneuses des Alpes Françaises (Col du Lautaret, Chamrousse) et dans la région Arctique (Sodankylä, Finlande). Au Col du Lautaret, la différence de température de surface de la neige mesurée entre les versants Nord et Sud était d'environ 6°C. A Sodankylä, la différence de température de surface de la neige entre les deux faces (Nord et Sud) d'une butte artificielle était de 4°C en moyenne sur la journée. De manière générale, il a été mesuré que les faces Nord des surfaces rugueuses était plus chaudes que celles exposées au Sud. La chaine de calculs développée dans cette étude permet de bien reproduire la différence de température entre les faces Nord et Sud des surfaces rugueuses et montre des résultats encourageants pour simuler les variations temporelles et spatiales de la température de surface de la neige. Une perspective d'amélioration de cette étude serait d'améliorer la résolution spatiale et temporelle des simulations pour permettre de mieux reproduire les variations observées sur le terrain.

Mots-clés : rugosité – température de surface de la neige – bilan radiatif – ray-tracing – variations temporelle – variations spatiale

Abstract

Snow-covered surfaces are generally represented in snow models as flat and smooth surfaces. In reality, the presence of roughness may introduce some biases in simulations of the evolution of the snowpack. Roughness features can be at different scales, from meter-scale (e.g. sastrugi, snow dunes) to kilometric scale (topographic hillsides). By trapping photons between roughness walls, roughness features can have a strong effect on snow surface temperature T_s, and so on the radiative balance at the surface. However, this effect is still poorly known and modeled. A Monte-Carlo ray-tracing model called RSRT was recently developed at the IGE to simulate the interactions between the sunlight and rough surfaces. This study aims to 1) measure the temporal and spatial effects of roughness on T_s, and 2) develop a computational chain to estimate T_s over rough surfaces based on the outputs of RSRT. Three field campaigns were organized during winter 2019 to quantify spatial and temporal T_s variations in mountainous areas in the French Alps (Col du Lautaret and Chamrousse) and in the Finnish Arctic (Sodankylä). At the Col du Lautaret site, the difference in T_s measured in the field between the northern and southern faces of the mountains was about 6°C. At the Sodankylä site, the average difference in T_s between the northern and southern face of a meter-scale artificial rough feature was about 4°C during the day. T_s estimations were compared to measurements. Generally, the northern faces of the rough surfaces were measured cooler than the southern ones. The developed chain well reproduces the difference in T_s between northern and southern faces and show promising results to simulate the temporal and spatial variations of T_s over roughness at different scales. A perspective of improvement is to refine the simulations at a smaller temporal and spatial scale, in order to improve the agreement between simulations and measurements.

Keywords: roughness – snow surface temperature – radiative balance – ray tracing – temporal variations – spatial variations

TABLE OF CONTENTS

1. INTRODUCTION

From high altitude areas to polar regions, snow cover represents more than 30% of the Earth surface during winter in the Northern Hemisphere. Because it is the most reflective surfaces on Earth (Gallet et al., 2011, Carmagnola et al., 2013), its presence on the ground plays a crucial role in the surface energy budget and cools the underlying layers of the atmosphere relative to other surfaces (Barry, 2002, Vavrus, 2007, Armstrong and Brun, 2008). Understanding the effects of reflection and absorption of the sunlight over snow-covered surfaces is critical to predict the evolution of the snowpack for climate previsions (Lucht et al., 2000, Adams et al., 2011), or, at smaller scales, for avalanche forecasting and hydrological processes (Brun et al., 2012, Vionnet et al., 2012, Jamieson and Schirmer, 2016).

The surface energy budget describes the fluxes exchanged between the surface and the atmosphere (Etchevers et al., 2004), including: (i) turbulent fluxes, corresponding to sensible and latent heat fluxes (Male and Granger, 1981, Kiehl and Trenberth, 1997) and (ii) radiative fluxes. The net radiative flux is the sum of the surface shortwave net radiation, from 0.35 µm to approximately 4 µm, and the surface longwave net radiation, from 4 µm to 20 µm (Ambach, 1974, Van den Broeke et al., 2004, Pomeroy et al., 2016), with the net flux describing the difference between the downward and the upward fluxes. The upward longwave flux is governed by the snow surface temperature (noted T_s) through the Stefan Boltzmann law (Van den Broeke et al., 2004, Shea and Jamieson, 2011, Li et al., 2016) and the upward shortwave flux is governed by the snow surface albedo, defined as the proportion of incoming solar radiation reflected by the surface (Dumont et al., 2010, 2011). These two parameters (T_s and snow albedo) are major players in the radiative balance and energy budget of snow surfaces (Brun et al., 2011, Raleigh et al., 2013).

Snow albedo governs the amount of radiation absorbed at the surface: the radiation not reflected by the surface is absorbed (absorption = 1 − albedo). Snow surface albedo, and thus absorption, mainly depends of the snow properties at the surface (i.e. snow grain size and microstructure, concentration of impurities) (Aoki et al., 2007), the tilt of the surface (i.e. slope elevation and orientation) (Dumont et al., 2011, Wang et al., 2016), the atmospheric composition (i.e. cloudiness, aerosol content) (Ambach, 1974, Carroll and Fitch, 1981, Aoki et al., 1999) and the illumination conditions (direct, diffuse) (Warren, 1982). The latter includes the angle between the zenith and the incident solar angle, called solar zenith angle (noted θ_s), and the sun orientation with respect to the North, called solar azimuth angle (noted φ_s). These dependencies on the snow albedo have been studied in details and are taken into account in snowpack modelling (Warren and Wiscombe, 1980, Wiscombe and Warren, 1980, Brun et al., 1989, 1992, Vionnet et al., 2012, Tuzet et al., 2017). However, the snow surface is generally represented in these models as flat and smooth while it usually exhibits roughness features and is tilted in mountainous regions. Roughness here is taken

as a general-scale independent term to refer to any sub-footprint variations of surface elevation (or altitude), from meter-scale (e.g. sastrugi, snow dune) to kilometer-scale (e.g. topographic hillsides). These rough features have two effects: (i) the local solar zenith angle (noted θ'_s) on the surface is different than θ_s, and (ii) an increased trapping of photons in the cavities of the roughness (Warren et al., 1998). These two effects lead to a decrease of snow spectral albedo (Kuchiki et al., 2011, Lhermitte et al., 2014), and in turn an increase of absorption. By modifying the snow albedo, and by introducing multiple reflections, surface roughness can have a high impact on the radiative balance (Plüss and Ohmura, 1997, Lee et al., 2019), and subsequently on the T_s of the snowpack. However, very few studies have quantified this phenomena (Dozier, 1980, Dubayah et al., 1989). The objective of this master thesis is to estimate by in-situ observations and modeling the impact of the roughness on surface temperature.

A possible approach to account for surface roughness in optical models is to use a Monte Carlo photon transport algorithm. A 3D mesh representing the terrain elevation in the studied area is given as input, and an ensemble of photons (i.e. particles of light) is launched onto the surface to simulate the interactions between sunlight and rough features. Lee et al. (2019) used this approach to simulate the solar energy absorbed by a snow surface at the scale of a climate model (hundreds of kilometers) considering the effect of the sub-pixel topography over the Tibetan Plateau. They concluded that (i) the impact of topography on the surface energy budget is critical over areas with complex terrain, and (ii) taking into account the effect of topography would improve the global climate previsions of surface air temperature by 13%, highlighting the importance to better understand and model the effects of roughness in the energy budget. However, their study focused on the energy budget at the surface, but did not investigate the impact on T_s.

Recently, a new model has been developed at the IGE by G. Picard and F. Larue to simulate snow albedo over a rough surface. Called Rough Surface Ray Tracing (RSRT), this model computes the photon path from the radiation source to termination (either escaping the scene or being absorbed) to retrieve the attenuated final intensity of the photon source with a Monte Carlo algorithm (Larue et al., in prep.). For each facet of the 3D mesh, the number of photons hitting the surface is computed. In the last version, RSRT also accounts for the re-illumination of each facet towards neighbouring facets. This model therefore accounts for all the 3D geometric effects. The objective of this thesis is to estimate T_s for each facet from the outputs of RSRT and using the radiative balance. At this stage, the turbulent fluxes are neglected.

This study has two aims: (i) measure the variations of T_s over different rough surfaces, at different scales (meter-scale and topographic), and (ii) improve the RSRT model in order to simulate T_s, and then evaluate its output in various terrain configurations. T_s measurements were acquired during winter 2019 in the French Alps to study effects of the topography and in the Finnish Arctic over a

surface with meter-scale roughness features. These observations were used to quantify T_s variations, and were compared to RSRT simulations to evaluate the quality of the model.

The bases of the surface radiative balance are detailed in Section 2. This section also contains a description of the models used in this study, and presents the field data gathered during winter 2019. The results of the data analysis and of the evaluation of RSRT are provided in Section 3. The latter results are discussed in Section 4. Concluding remarks are given in Section 5.

2. METHODS AND DATA

2.1. Bases of radiative balance

The equation of the energy budget is written as follows (Weller, 1969, Van den Broeke et al., 2005, Pomeroy et al., 2016) :

$$R_{net} + H + L + G = 0 \qquad [1]$$

where H is the sensible heat flux, also defined as the heat exchanged between the surface and the atmosphere associated with a temperature change of the body; L is the latent heat flux, described as the heat transferred to or away from the surface associated with a phase change of the body; G is the ground heat flux, representing the heat transferred through the underlying body (for a snow surface, the underlying body is the snowpack below the surface); R_{net} is the net radiation, representing the gain or loss of radiation by the surface, and expressed as the sum of the net shortwave and longwave radiation fluxes. We have neglected here advection terms, for instance the energy associated to snowfall or rain. All the fluxes are expressed in Wm^{-2}.

In this study, we only consider only the radiative flux based on the following arguments: G is close to zero assuming the snowpack is considered thermalized, such that no energy is lost away from the surface in the underlying layers of snow. L and H are also neglected, considering relative stable conditions as it is the case in the morning with anticyclonic conditions when the impact of roughness on T_s is though to be maximum. This also corresponds to when the field measurements were conducted.

Hence, [1] can be expressed as a radiative balance only, and expressed as follows:

$$R_{net} = SW_{net} + LW_{net} = 0 \qquad [2]$$

where SW_{net} represents the shortwave net radiation in the 0.35 - 4 µm range of the electromagnetic spectrum, and LW_{net} is the longwave net radiation flux in the 4 - 20 µm range. These two components are expressed as follows:

$$SW_{net} = SW_d - SW_u \qquad [3]$$

$$LW_{net} = LW_d - LW_u \qquad [4]$$

with SW_d and SW_u the downward and upward shortwave fluxes, and LW_d and LW_u the downward and upward longwave fluxes, respectively. These terms are expressed as integrated values over their respective spectral ranges.

SW_d and LW_d correpond to the downward radiations coming to the surface from the sun and the atmopshere. SW_d can be decomposed in one direct and one diffuse component, written $SW_{d,dir}$, $SW_{d,diff}$. The direct term represents the radiation arriving on the surface without undergoing any reflection or absorption on its way, while the diffuse component is the radiation flux arriving on the surface after being scattered and or reflected by the surface (multiple reflection).

The upward flux SW_u is related to the downward flux SW_d through the albedo, following [5]:

$$SW_u = \alpha SW_d \tag{5}$$

In this study, snow is considered as a black body in the LW range, that absorbs all radiation (absorption = 1). Following Kirchoff law, the snow emission is therefore equal to 1. According to Stefan-Boltzmann law, LW_u can be expressed as a function of the LW_d and the absolute temperature, here considered as equal to T_s (in Kelvins), such as:

$$LW_u = \sigma T_s{}^4 \tag{6}$$

where σ is the Stefan-Boltzmann constant, equal to $5,6698.10^{-8}$ $Wm^{-2}K^{-4}$.

Bringing together equations [1] to [6], the radiative balance is expressed as follows:

$$(1-\alpha)(SW_{d,\,dir} + SW_{d,\,diff}) + LW_d = \sigma T_s{}^4 \tag{7}$$

All fluxes are expressed in Wm^{-2}.

Since radiations have spectral dependence, the spectral form of equation [7] used in this study for the radiative balance is expressed as follows:

$$\int_{0.3\mu m}^{1.2\mu m} \left(1 - \alpha_{dir}(\lambda, \theta_s)\right)Irr_{dir}(\lambda)\, d\lambda + \int_{0.3\mu m}^{1.2\mu m} \left(1 - \alpha_{diff}(\lambda)\right)Irr_{diff}(\lambda)\, d\lambda + LW_d = \sigma T_s^4 \tag{8}$$

with $Irr_{dir}(\lambda)$ and $Irr_{diff}(\lambda)$ the direct and diffuse solar spectral irradiance ($Wm^{-2}\mu m^{-1}$); $\alpha_{dir}(\lambda, \theta_s)$ and $\alpha_{diff}(\lambda)$ the direct and diffuse components of albedo; and θ_s the solar zenith angle. In case of a tilted terrain, $\alpha_{dir}(\lambda, \theta_s)$ depends on the effective solar zenith angle θ'_s instead of θ_s (Dumont et al., 2017). We limit this study to the use of a broadband LW_d.

2.2. Model description

Several models were used to simulate parameters needed to estimate T_s from [8]: 1) $Irr_{dir}(\lambda)$ and $Irr_{diff}(\lambda)$ were simulated with the atmospheric model SBDART (Section 2.2.1); 2) snow spectral albedo $\alpha_{dir}(\lambda, \theta_s)$ and $\alpha_{diff}(\lambda)$ with the Asymptotic Radiative Transfer theory (Section 2.2.2); 3) RSRT was run to simulate the number of collisions of photons on the mesh and used to compute

4

the absorption coefficient per facet (Section 2.2.3). Section 2.2.4 details the computational chain implemented to estimate T_s (Section 2.2.4).

2.2.1. SBDART

Santa Barbara DISORT Atmospheric Radiative Transfer (SBDART, Ricchiazzi et al., 1998), is an atmosheric model computing radiative transfer within the Earth's atmosphere and at the surface, in clear-sky and cloudy conditions. It is based on several reliable models to account for clouds, gas absorption and aerosols in atmpsheric layers, and for surface reflection and then to compute the radiative transfer (Ricchiazzi et al., 1996). The model provides six standard atmospheric profiles to model typical climatic conditions. More details on SBDART can be found in Ricchiazzi et al. (1996, 1998).

SBDART was used here to simulate spectral incoming direct and diffuse shortwave irradiances $Irr_{dir}(\lambda)$ and $Irr_{diff}(\lambda)$ according to the composition of the atmosphere and the illumination conditions. Simulations were run with appropriate atmospheric profile (i.e. according to location of field data), and appropriate solar zenith and azimuth angles (θ_s, φ_s) corresponding to when measurements were acquired. Spectral $Irr_{dir}(\lambda)$ and $Irr_{dir}(\lambda)$ were simulated every 4 nm in the 350 - 1202 nm range. For all experiments, the model was run in clear-sky conditions, with no aerosol layer. In addition to the direct and diffuse irradiances, SBDART provided the spectral diffuse-to-total ratio ($r_{diff-tot}(\lambda)$), corresponding to the proportion of direct irradiance compared to diffuse irradiance.

2.2.2. ART

The Asymptotic Radiative Transfer theory (ART) provides simple analytical formulation of radiative transfer for highly reflective material, which applies well to snow in the visible, near and even short wave infrared (Kokhanovsky and Zege, 2004). This theory is based on several assumptions to simulate snow spectral albedo (Kokhanovsky and Zege, 2004, Dumont et al., 2017): (i) the snowpack is represented as plane-parallel homogeneous layers, (ii) the surface of the snowpack is flat and smooth, (iii) the snowpack is semi-infinite and (iv) snow albedo depends on the Specific Surface Area of snow grains (SSA), and on two parameters representing the snow grain shape: the asymmetry factor g and the absorption enhancement parameter B. SSA is defined as the ratio between air-ice interface and mass of the ice in the sample, and is expressed in m^2kg^{-1} (Gallet et al., 2011, Carmagnola et al., 2013). B quantifies the lengthening of the photon path inside grains due to multiple internal reflections and g measures the ratio between forward and backward scattering by the grains (Libois et al., 2014b).

With these assumptions, the direct and diffuse components of albedo at wavelength λ and at θ_s, respectively $\alpha_{dir}(\lambda, \theta_s)$ and $\alpha_{diff}(\lambda)$ in [8], are estimated with the ART theory following equations [9] and [10] (Kokhanovsky and Zege, 2004):

$$\alpha_{\text{dir}}(\lambda, \theta_s) = \exp\left(\frac{-12(1 + 2\cos\theta_s)}{7}\sqrt{\frac{2B\gamma_\lambda}{3\rho_{\text{ice}}\text{SSA}(1-g)}}\right) \quad\quad [9]$$

$$\alpha_{\text{diff}}(\lambda) = \exp\left(-4\sqrt{\frac{2B\gamma_\lambda}{3\rho_{\text{ice}}\text{SSA}(1-g)}}\right) \quad\quad [10]$$

where B and g are assumed to be constant (B = 1.6 and g = 0.86, see Libois et al., 2014b), ρ_{ice} = 917 kgm^{-3} is the bulk density of ice at 0°C, and γ_λ is the wavelength dependent absorption coefficient of ice, taken from Picard et al. (2016).

Similar to the simulations of $\text{Irr}_{\text{dir}}(\lambda)$ and $\text{Irr}_{\text{diff}}(\lambda)$ with SBDART, $\alpha_{\text{dir}}(\lambda, \theta_s)$ and $\alpha_{\text{diff}}(\lambda)$ were simulated with the ART theory every 4 nm from 350 to 1202 nm. SSA measurements were acquired in the field (Section 2.3).

2.2.3. RSRT

RSRT was developed to simulate the propagation of a large number of photons launched on a rough surface, given as input and represented by a 3D mesh composed of a set of triangular facets. In order to get a good precision with the model (~3%), the total number of photons has to be high enough so that at least 1000 photons reach each facet.

Each photon carry an energy flux, and is described by its intensity, its origin *r*, and its propagation direction $\vec{\iota}$. Each photon is initialized with an intensity equals to 1 (unitless quantity of energy, scaling is performed outside, in the computational chain) and a direction $\vec{\iota}$. The initial direction $\vec{\iota}$ of the photon is given by the sun position described with the (θ_s, φ_s) couple, and randomly chosen in the diffuse configuration. To represent an infinite source, photons are quasi-uniformly distributed above the surface. To avoid edge effects, i.e. when photons are launched close to the boundaries of the mesh and rebound outside, without any chance they come back in the scene, a threshold is fixed to limit the footprint of the source so that 70% of the mesh and the most central part is actually hit by photons.

In the model, the path of each photon is computed in four main steps: (1) estimate the next intersection between the mesh and the photon (called 'hit'), (2) update the intensity after the hit, (3) sampling outgoing direction and (4) update the direction. The flowchart of a photon path in RSRT can be found in Appendix 1 (Larue et al., in prep.). These steps are further described.

The first step searches for the first facet of the mesh on the photon propagation path. If there is a hit, the origin *r* of the photon is updated on the hit facet.

When a photon hits the surface, it loses energy and the intensity of the photon is reduced by a factor (1 - albedo) (step 2).

In this study, the facets of the mesh are considered as Lambertian surfaces, meaning that facets reflect light with the same intensity in each direction ('Lambertian' configuration, i.e. ideal diffusion). Considering that the facets of the mesh reflect the light equally in all directions, the outgoing direction of the photon after the hit with the mesh is randomly picked with a cosine-weighted hemispherical distribution (steps 3 and 4).

Until the photon escapes the scene, the algorithm returns to the first step. In case of a low intensity of the photon (intensity < 0.01), a 'Russian roulette' is applied to ensure an unbiased termination. This is done by either accepting or rejecting the termination, with probability $1-p$ and p respectively (with p=0.2). In case of rejection, the intensity is increased by $1/p$ and the photon continues its trajectory.

At the end of its path, each photon has hit the mesh one or several times. Its final intensity contributes either to the total upward intensity (if last $\vec{\iota}$ directed upward) or to the intensity lost downward (if last $\vec{\iota}$ directed downward, it can be the case with tilted surfaces). The model outputs the number of hits per facet, according to its order of hit (i.e. if it is the 1st, 2nd ... 14th hit of the photon, and last is 15th or more). Noted $n_{hit,i}$, with i between 1 and 15, this number corresponds to the proportion of the total number of photons launched onto the mesh that hit the facet on their ith hit, and is between 0 and 1.

Each simulation includes two runs: one in direct illumination and one in diffuse illumination conditions to ouput $n_{hit,dir,i}$ and $n_{hit,diff,i}$ respectively. The number of photons launched onto the surface is set to 100.10^6.

The following table summarizes the inputs of RSRT in the Lambertian configuration:

Inputs	Description
θ_s	Zenith angle of the radiation source (°)
φ_s	Azimuth angle of the radiation source (°N) and clockwise
Mesh	Triangular mesh of the 3D scene
Mesh orientation	Azimuthal orientation of the mesh around the z axis (°N)
$N_{photons}$	Size of the photon ensemble

Table 1: RSRT inputs description in Lambertian configuration (adapted from Larue et al., in prep.).

A naive approach would be to use RSRT to compute the absorbed radiation for every wavelength in the solar spectrum range, but this would be very time consuming. We have devised an alternative and much faster approach, possible with the Lambertian approximation, where we estimate the absorbed radiation by facet outside of the model, using the n_{hit} output. The method is described in the following Section 2.2.4.

2.2.4. Snow surface temperature estimation

A computational chain was established to process the number of hits predicted by RSRT under different illumination conditions into T_s. The chain consists in simulating all parameters needed to estimate T_s based on Equation [8] described in Section 2.1. The surface temperature T_s of each facet is computed in eight steps illustrated in Figure 1.

Step 1: Absorption coefficient for each facet. The absorption coefficient of a facet in direct and diffuse illumination conditions (respectively $abs_{dir}(\lambda, \theta_s)$ and $abs_{diff}(\lambda)$) are calculated in the 350 - 1202 nm range, each 4 nm, following equations [11] and [12]:

$$abs_{dir}(\lambda, \theta_s) = \left(1 - \alpha_{dir}(\lambda, \theta_s)\right) \sum_{i=0}^{i=15} \alpha_{dir}^i(\lambda, \theta_s) n_{hit,dir,i} \qquad [11]$$

$$abs_{diff}(\lambda) = \left(1 - \alpha_{diff}(\lambda)\right) \sum_{i=0}^{i=15} \alpha_{diff}^i(\lambda) n_{hit,diff,i} \qquad [12]$$

where $n_{hit,dir,i}$ and $n_{hit,diff,i}$ the number of hits on the facets computed with RSRT respectively under direct and diffuse illumination.

Step 2: Spectral net shortwave radiation. The direct and diffuse spectral SW_{net} (Wm^{-2}nm^{-1}) are calculated following [13] and [14]:

$$SW_{dir}(\lambda, \theta_s) = abs_{dir}(\lambda, \theta_s) Irr_{dir}(\lambda) \qquad [13]$$

$$SW_{diff}(\lambda) = abs_{diff}(\lambda) Irr_{diff}(\lambda) \qquad [14]$$

Step 3: Broadband net shortwave radiation (SW_{net}). The results of step 2 are integrated over the 350 - 1202 nm wavelength range, following [15] and [16]:

$$SW_{dir}(\theta_s) = \int_{0.3\mu m}^{1.2\mu m} SW_{dir}(\lambda, \theta_s) \, d\lambda \qquad [15]$$

$$SW_{diff} = \int_{0.3\mu m}^{1.2\mu m} SW_{diff}(\lambda) \, d\lambda \qquad [16]$$

SW_{net} is calculated following [17]:

$$SW_{net}(\theta_s) = SW_{dir}(\theta_s) + SW_{diff} \qquad [17]$$

Step 4: Upward longwave radiation (LW_u). LW_u is calculated following [18]:

$$LW_u(\theta_s) = SW_{net}(\theta_s) + LW_d \qquad [18]$$

Step 5: Surface temperature (T_s). Steps 1 to 4 give the necessary elements to close the radiative balance and deduce the surface temperature T_s of each facet following equation [8] (Section 2.1).

Step 6: Viewing factor and re-illumination. The steps above considers that all facets of the mesh receive the longwave radiation from the sky as if they were flat. In reality, with roughness features, facets see partially sky and partially other facets. To account for this effect, the viewing factor V of each facet is obtained from RSRT. In fact, this V factor is equal to the proportion of photons hitting the facet on their first hit in diffuse illumination ($n_{hit,diff,1}$). In addition, each facet emits

8

longwave radiation as predicted by Stefan-Boltzmann law for its own T_s. In rough terrain, part of this radiation is emitted towards the other facets. This leads to an issue because T_s is needed to compute this term, which is itself needed to compute T_s. We propose a simple 'first order' solution: the re-illumination assumed constant for all facets and equals to the average longwave radiation emitted by all facets of the mesh due to their temperature calculated at step 5, that is when neglecting the sky view factor. This term is noted $LW_{u,mean}$.

The update longwave radiation flux $LW_{d,updated}$ takes into account the viewing factor of each facet, and the re-illumination of the scene with the facet temperatures as follows, for each facet:

$$LW_{d,updated} = VLW_d + (1-V)LW_{u,mean} \tag{20}$$

Steps 4bis and 5bis. Net radiation and surface temperature are re-computed with $LW_{d,updated}$ in equation [8] following steps 4 and 5.
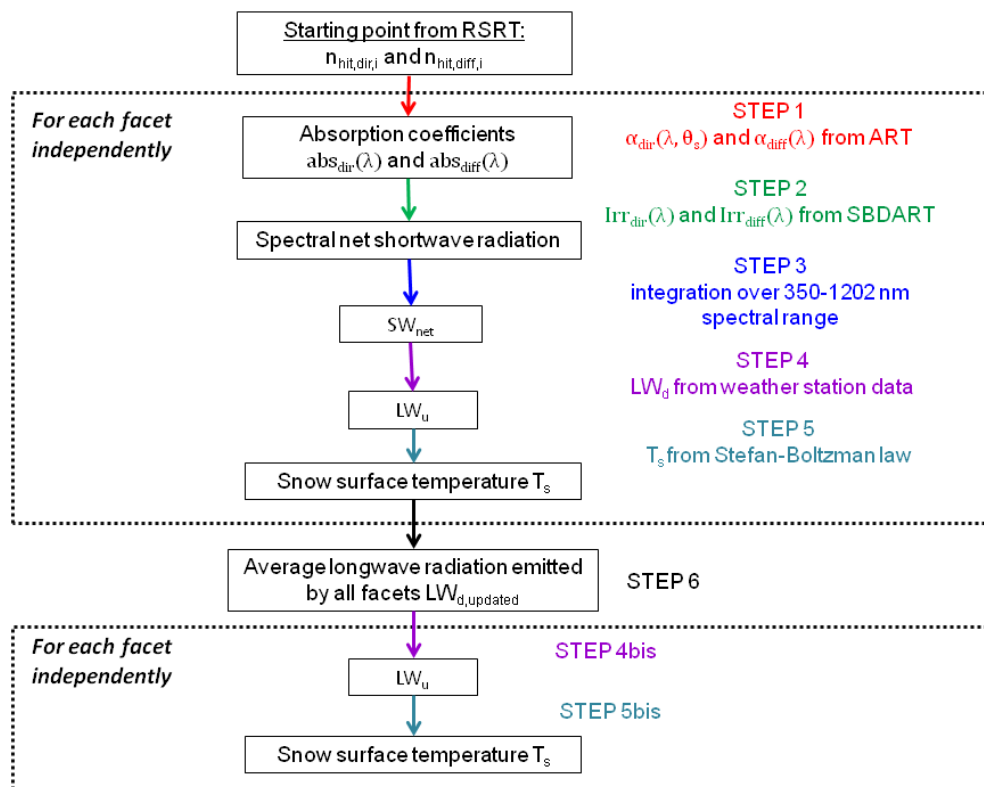

Figure 1: Flowchart of the developed computational chain to process the number of hits on a facet into T_s. The starting point is the ouput of the RSRT model. The method incorporate simulated variables from SBDART and ART models (irradiance and albedo in steps 1 and 2). The illustrated steps are detailed in Section 2.2.4. Steps 4bis and 5bis are equivalent to steps 4 and 5, but with the use of $LW_{d,updated}$.

2.3. Field campaigns and data description

During winter 2019, three field campaigns were conducted in different terrain configurations in the French Alps and the North of Finland. Data were collected in order to investigate and quantify the variations of T_s in rough terrain, at small and large scale.

2.3.1. Instrument description

Snow surface temperature (T_s). T_s was measured in the field with two Infrared Remote Temperature sensors (IR120) by Campbell Scientific (Web1, viewed May 2019). The IR120 includes a thermopile that measures thermal radiation in the 8 - 14 µm wavelength range. The thermopile detector gives a voltage proportional to the thermal energy balance between itself, and the detected surface. Based on the amount of thermal energy radiated by the surface, T_s is given using the Stefan-Boltzmann law. This requires the knowledge of the emissivity of the target: in this study, the emissivity of snow was set to 1. The IR120 has a large field of view, with a half-viewing-angle of 20°. The temperature is measured with a precision of ± 0.2°C (Web1, viewed May 2019), but due to the uncertainty on emissivity, absolute precision is of the order of 2°C.

In the field, two IR120 probes were used in parallel. In a cold room, a cross calibration was performed between the two probes and absolute calibrations for each probe at four different temperatures (-20°C, -10°C, -5°C and 0°C). The probes were vertically placed looking at a square metal plate thermalized at room temperature, and three successive temperature measurements were collected with each probe. For the absolute calibration, the metal plate absolute temperature was measured with a PT100 sensor (Campbell Scientific, Web2, viewed May 2019). Three linear regressions were estimated to relate: 1) the PT100 and the probe 1 (P1); 2) the PT100 and the probe 2 (P2) and 3) the calibrated data of P1 and P2. First, the temperature given by P1 was calibrated according to the absolute temperature applying the first linear regression to the temperature data of P1 (blue equation in Figure 2). The temperature measured by P1 was close to the absolute temperature, with a R^2 of 0.98. The same approach was applied for the second probe P2 applying the second linear regression on the temperature data (light blue equation in Figure 2). The temperature measured by P2 was close to the absolute temperature, with a R^2 of 0.96. The third linear regression was applied on the temperature data given by P1 (red equation in Figure 2). The temperature given by calibrated P1 was close to the temperature given by calibrated P2, with a R^2 of 0.99.

Figure 2 shows the results of the cross and absolute calibrations carried out in the cold rooms, including the equations used to calibrate the temperature data given by the sensors.

Specific surface area (SSA). SSA was measured in the field in the purpose of simulating snow spectral albedo with realistic values. SSA was measured using the Alpine Snowpack Specific Surface Area Profiler (ASSSAP, Arnaud et al., 2011). The accuracy of the instrument is 10-15%. The measurement is based on the shortwave infrared (SWIR) reflectance: a laser diode operating at 1310 nm illuminates the snow and the reflected radiance is measured at different angles. A second laser diode operating at 810 nm permits to evaluate the distance of the sample to the snow. Combining both the SWIR reflectance and the distance, the SSA is estimated using a theoretical formulation based on an asymptotic solution of the radiative transfer equation. The snow surface is sampled and placed in front of the laser diodes. Several acquisitions are taken

while slowly turning the sample to assess its heterogeneity, and the SSA value is taken as the average over the acquisition time.
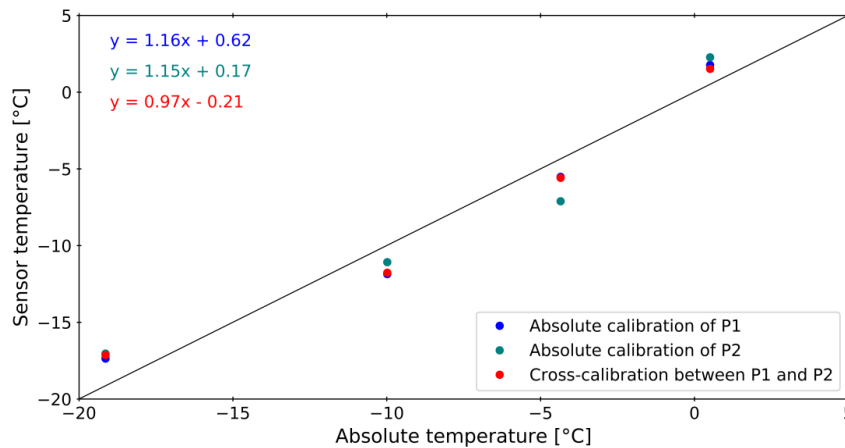

Figure 2: Temperatures measured by two probes (sensor temperature) as a function of absolute temperature. Blue points are P1 data after the absolute calibration, green points are P2 data after the absolute calibration and red points are the P1 data after the cross-calibration.

2.3.2. Framework of field experiments

Table 2 summarizes measurements acquired in the field and input data used for RSRT simulations for the three experiments described further. Simulations were performed in order to reproduce the field conditions encountered during the different experiments.

Meter-scale roughness: Chamrousse, French Alps and Sodankylä, Finnish Arctic. Two sites were selected to study the temporal variations of T_s over artificially created meter-scale rough surfaces. The Chamrousse experiment was conducted to test the T_s estimation method developed in this study.

The site of Chamrousse is located in the French Alps, near Grenoble (45.111°N, 5.875°E, 1730 meters a.s.l). This site was chosen mainly because of its accessibility from the laboratory and offered an open and flat snow area to make our first experiments.

Measurements of T_s were acquired on February 22nd, over a rough surface artificially created on an initial flat zone of 2.5 x 2.5 m^2. The studied surface is illustrated in Figure 3. Linear rough features were produced by pressing a triangular wooden bar, regularly spaced with a period of 11 cm, and 7 cm deep. The rough features were created with an azimuthal orientation East-West, so that some parts of the roughness walls facing North were always in the shadow, and some parts facing South were always illuminated. T_s measurements were taken simultaneously on the northern walls of the rough surface with one probe and on a smooth surface nearby the rough surface with the second probe, between 09:48 and 16:14 (UTC) (see Figure 3 and Table 2). The mesh used for RSRT simulations was created with the same geometry as in the field, and is shown in Figure 3.

	Measurements	**Simulations**
Chamrousse		
Date, hour for T_s (UTC)	February 22nd 2019 09:48 – 16:14 (every 20 second)	February 22nd 2019 12:00
θ_s, φ_s	75° – 55°; 121°N – 231°N	57°, 165°N
SSA (m^{2}kg^{-1})	N/A	15
LW$_d$ (Wm^{-2})	N/A	210
Sodankylä		
Date and hour for T_s (UTC)	March 26th 2019 06:00 – 22:00 (every 20 second)	March 26th 2019 08:00 – 17:00 (every hour)
θ_s, φ_s	90° – 65°; 84°N – 323°N	78° – 65°; 113°N – 252°N
SSA (m^{2}kg^{-1})	20 – 40	30
LW$_d$ (Wm^{-2})	200 – 271	255
Col du Lautaret		
Date and hour for T_s (UTC)	February 26th 2019 08:12 – 12:36 (every 20 second)	February 26th 2019 09:00; 11:00; 13:00
θ_s, φ_s	83° – 54°; 109°N – 184°N	74° – 54°; 121°N – 184°N
SSA (m^{2}kg^{-1})	5 – 30	15
LW$_d$ (Wm^{-2})	234 – 246	265

Table 2: Measurements and simulations description for the experiments at the Chamrousse, Sodankylä and Col du Lautaret sites. The LW$_d$ values corresponds to data from weather stations near the sites (FluxAlp for the Col du Lautaret and FMI data for Sodankylä). Local hour at Chamrousse and Col du Lautaret: UTC+1, local hour at Sodankylä: UTC+2.

Simulations were perfomed for February 22nd, at 12:00 UTC, with an SSA of 15 m^{2}kg^{-1} and a LW$_d$ of 210 Wm^{-2}. At this hour, θ_s was equal to 57° and φ_s to 165° (see Table 2). Unfortunately, LW$_d$ was not available. This is why this experiment has only be used to test the coherence of our developed approach, and not for validation.
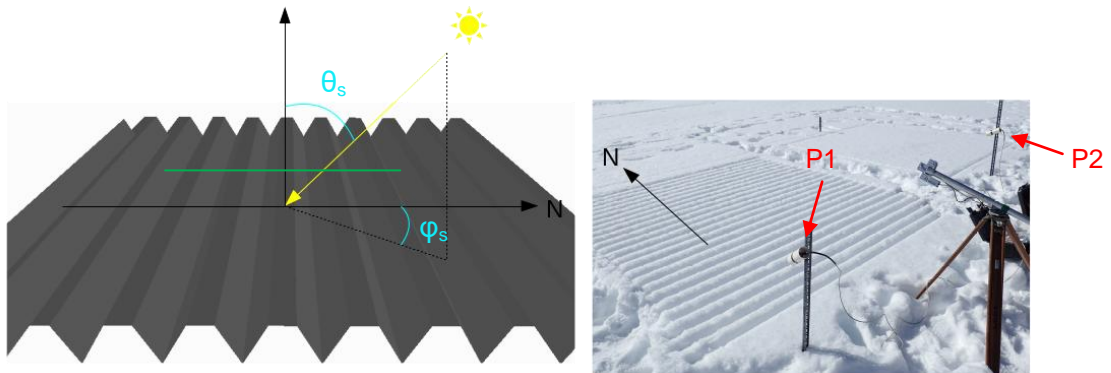

Figure 3: Mesh of the Chamrousse experiment (left). Artificial rough surface in the field (right). The IR120 probes P1 measuring T_s of the northern walls of the roughness features and P2 measuring T_s of the smooth surface are visible in the picture (indicated by the red arrows). The green line represents a cross-section throught the rough surface. The sun position is given by θ_s and φ_s.

The site of Sodankylä is located in the Finnish Arctic region (67.367°N, 26.652°E, 180 meters a.s.l.). The Finnish Meteorological Institute (FMI) is partly based there with significant infrastructure dedicated to snow, and especially has a well instrumented measurement site. Longwave radiation is measured every 10 min at the height of 45 m by a Kipp & Zonen CNR4 net radiometer installed on meteorological mast situated approximately 1 km away from the experiment site (data from FMI, available at Web3, viewed April 2019). This instrument provided the LW_d values needed to perform the simulations.

A field campaign for snow measurements was organized by the FMI there in March 2019 to intercompare radiospectrometer instruments to measure spectral albedo. IGE was invited and I had the opportunity to participate to this community effort, to gain a wider experience on snow radiation. I also had the possibility to devote part of my time on studying the temporal variations of T_s according to the sun exposition as described here.

Measurements were acquired over a mound artificially created (Figure 4). The mound was 40 cm high, 1 m long, with an inclination of about 40° on both sides, and with an azimuthal orientation East-West, so that the sides were facing North and South. T_s measurements were taken simultaneously on both sides of the mound (one IR120 probe looking at the northern face and the second one looking at the southern face, see Figure 4) during five days (from March 25th to 29th) and every 20 seconds 24 hours a day. The data of March 26th from 06:00 to 22:00 (UTC) only was used for data analysis, because of the clear-sky conditions, absence of precipitation, low air temperature and light wind. The other days were warm and overcast. The surface SSA values were measured in the field with ASSSAP over a flat area near the snow mound and on the walls of the mound. SSA values were ranging between 20 and 40 m^2kg^{-1} (see Table 2).
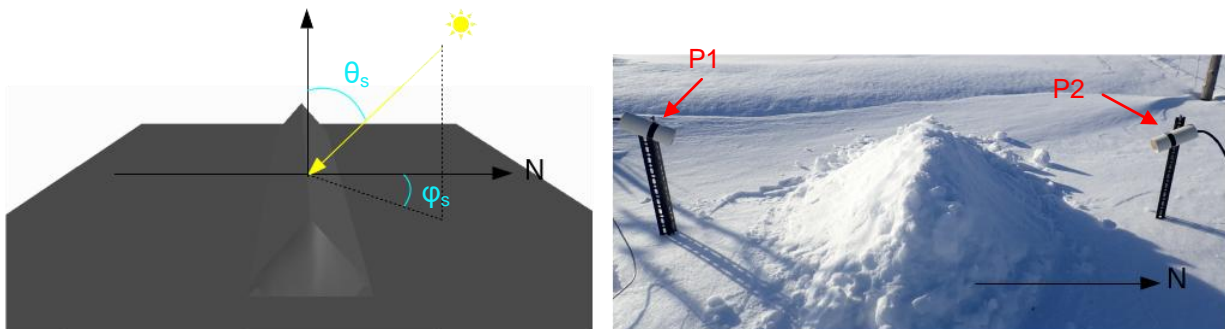

Figure 4: Mesh of the Sodankylä experiment (left). Artificial mound in the field (right). The two IR120 probes measuring T_s on southern and northern faces are visible in the picture (P1 and P2 indicated by the red arrows).The sun position is given by θ_s and φ_s.

The mesh needed to run RSRT was built according to the geometry of the artificial mound, and is shown in Figure 4. Simulations were perfomed for March 26th, every hour between 08:00 and 17:00 UTC, with a constant SSA of 30 m^2kg^{-1} and a constant LW_d of 255 Wm^{-2}. This was chosen in the range of values given by the FMI observations for that day, so that the resulting simulated T_s

was in the right order of magnitude of the measured T_s. θ_s was ranging from 65° to 78° and φ_s from 113°N to 252°N (see Table 2).

Topographic scale: Col du Lautaret, French Alps. The Col du Lautaret is located in the French Alps, southeast of Grenoble (45.042°N, 6.410°E, 2050 meters a.s.l). It was chosen to analyse the spatial variation of T_s data according to the topography and because it is a tree-free terrain, which made measurements easier. The site is also well instrumented, with a weather station called FluxAlp that measures every 30 min a lot of variables, including downward and upward shortwave and longwave radiation fluxes. The radiation fluxes are measured with a Kipp & Zonen CNR4 net radiometer (Laurent et al., 2014). This weather station provided the LW_d values used to perform the simulations.

On February 26th, between 08:12 and 12:36 (UTC), T_s measurements were collected along a transect around the site, every 20 second (corresponding to approximately 10 m in distance along the transect), with both IR120 probes. The probes were installed on a fixed bar on both sides of a backpack, looking down at the surface (see Figure 5). A quality flag was associated with each measurement of P1 and P2, to later process the data. The quality of the measurement was estimated based on the field experience: the measurement was good when the probe was not viewing any sky, any snow-free surfaces, any shadow from the person carrying the backpack or other items (such as skis or poles used to move along the transect). When the measurement quality of both probes was good, the final measured T_s was calculated as the mean of the T_s measured by P1 and P2. If the quality of both measurements were not good, the acquisition was discarded. If T_s from either probe had a good quality, the measurement corresponding to the valid probe was kept.

The path for the transect was chosen to capture topographic variations, and was recorded with a GPS (Global Positioning System), so that each T_s measurement is associated with latitude and longitude. The GPS used was a portable device, with an accuracy of 5 to 10 m. SSA measurements were also acquired along the transect with ASSSAP. These measurements were combined with the T_s measurements so that each point of measured T_s was associated with a value of SSA (see Table 2).

The mesh used for RSRT simulations was built from a Digital Elevation Model (DEM) provided by ASTER (Advanced Spaceborne Thermal Emission and Reflection Radiometer, NASA, data available at Web4, viewed February 2019). This DEM was acquired in snow-free conditions and has a resolution of 30 m. The resulting mesh is made of triangular facets, with a spatial resolution of 30 m as well, and covers the area where the T_s measurements were conducted. Simulations were performed for February 26th, at 09:00, 11:00 and 13:00 (θ_s = 74°, 59°, 54° and φ_s = 121°N, 149°N, 184°N, respectively). All three simulations were performed with a constant SSA of 15 m^2kg^{-1} and a constant LW_d of 265 Wm^{-2} (see Table 2). LW_d was adjusted from the FluxAlp data so that the resulting simulated T_s covers the measured T_s along the transect. It is important to note

14

that RSRT does not taken into account the attenuation and emission over the path in the atmosphere between the facets, which can in this case of the topographic scale be of hundreds of meter to kilometers, and may have a non negligible effect.

Figure 5: Set up for T_s measurements along the transect at Col du Lautaret. The two IR120 probes were facing the snow surface (P1 and P2 indicated by the red arrows). Measurements were acquired every 20 second on the transect, which corresponds to a distance of 10 m on the transect, on February 26th, between 08:12 and 12:36 (UTC).

3. RESULTS

The results are presented for the three sites, with different purpose adapted to the experiments. Section 3.1 presents the results from the Chamrousse. Section 3.2 presents the results of the temporal variations of measured and simulated T_s at the Sodankylä site. Section 3.3 presents the spatial variations of T_s measured and simulated at the Col du Lautaret.

3.1. T_s estimation method

The experiment conducted at the Chamrousse site was used to evaluate the retrieval method of T_s combining the outputs of the models SBDART, ART and RSRT (see flowchart in Figure 1).

The parameters SW_{net}, LW_u and T_s were respectively estimated with steps 3 to 6, 4bis and 5bis detailed in Section 2.2.4 and illustrated in Figure 1. Figure 6 shows spatial variations of these simulated parameters and the elevation, extracted along a cross-section perpendicular to roughness features (green line in Figure 3).

The cross-section profile is displayed with the black line in Figure 6a, showing the flat, northern and southern parts of the studied surface.

Figure 6b shows SW_{net} variations, and ranging from 4 to 85 Wm^{-2}, with flat areas of the cross-section absorbing 44 Wm^{-2}. The minimum SW_{net} is observed as expected on the northern faces of the cross-section, and the maximum to the southern faces. The north-facing walls of the roughness features receive less shortwave radiation from the Sun because the illumination comes from the South ($\varphi_s = 165°N$) at a low angle ($\theta_s = 57°$).

Figure 6c shows the LW_u emitted by the facets (step 4 in Section 2.2.4) before and after the consideration of the viewing factor V (step 4bis). Without considering V, LW_u varies from 214 to 295 Wm^{-2}, with the flat areas emitting 254 Wm^{-2}. By updating the LW_u with the V factor, LW_u varies from 234 to 311 Wm^{-2} along the cross-section. For both cases, the minimum corresponds to the northern faces and the maximum to the southern faces. With the V factor, the facets receiving LW_d from the sky and LW_u emitted by surrounding facets are warmer than those receiving LW_d from the sky only, since surrounding facets are warmer than the atmosphere (sky). This effect is well visible in Figure 6c: by considering V, the northern and southern faces emit more LW_u than without considering V.

Figure 6d displays the temperature T_s of the rough surface along the transect, estimated without and with the V factor. Without accounting for V, T_s varies from -25°C in the northern faces to -5°C in the southern faces. When accounting for V, T_s varies from -20°C (northern faces) to -1°C (southern faces). The temperature of the flat and uppermost facets of the mesh do not change when V is accounted for (facets see sky only) because V = 1, and is of -14.5°C. The figure shows a warming of the cavities of the mesh (concave parts) when V is accounted for compared to when it is not. The difference in T_s without and with the viewing factor along the cross-section is ranging from 0°C (flat areas) to 6.8°C (bottom of cavities), with an average of 2.9°C showing that the re-illumination tends to heat the surface. This warming in the cavities is due to the surrounding facets that emit LW_u according to their T_s.

The enhenced absorption in the cavities of the mesh shown with this results is coherent with what was found in previous studies (Kuchiki et al., 2011, Lhermitte et al., 2014) and the trapping effect predicted by Warren et al., (1998) was also shown with these results.

The estimation method of T_s developed in this study reproduces well the two phenomena above for the Chamrousse experiment and appears to be satisfying.
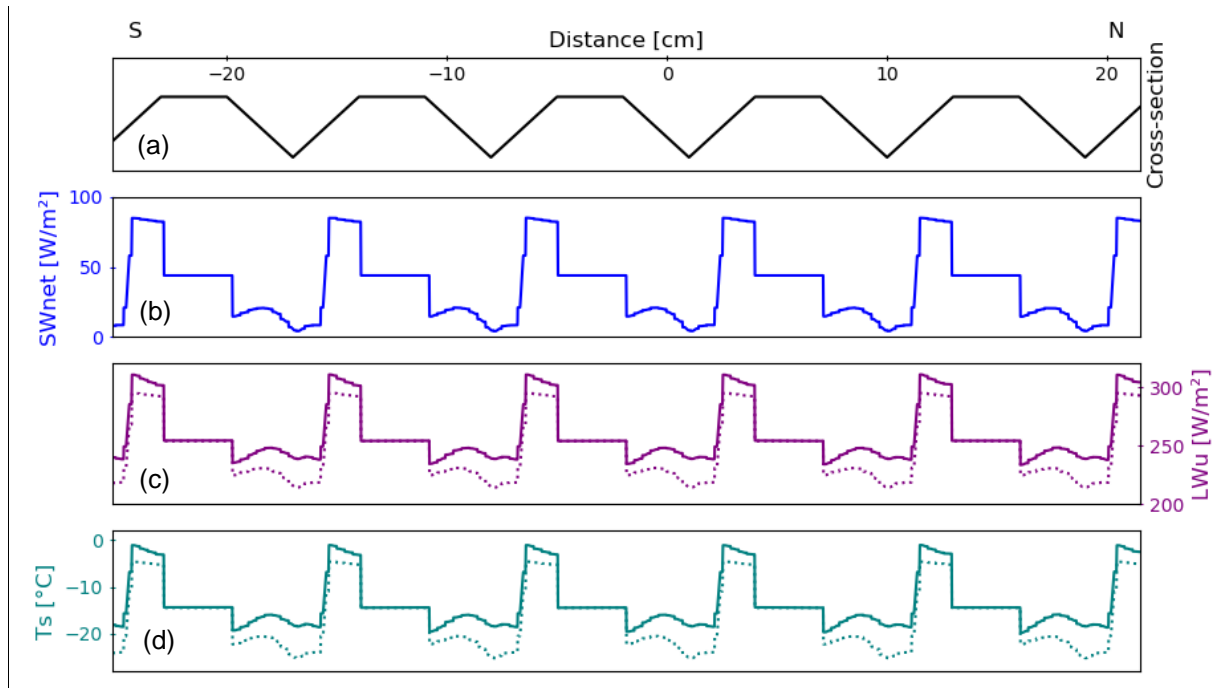
Figure 6: Spatial variations of (b) net shortwave radiation (step 3 in Section 2.2.4) in blue (Wm^{-2}), (c) upward longwave radiation (step 4 in Section 2.2.4) in purple (Wm^{-2}) and (d) T_s (step 5 in section 2.2.4) in light blue (°C). Dotted lines show simulated parameters without considering the viewing factor V, full lines show the simulation results with the V factor (step 4bis and 5bis in section 2.2.4). The parameters were simulated with SBDART, ART and RSRT over the entire mesh, and data were exctracted along a cross-section perpendicular to roughness features at the Chamrousse site (profile shown in (a)), on February 22th, at 12:00 (UTC), $\theta_s = 57°$ and $\varphi_s = 165°N$, $LW_d = 210$ Wm^{-2} and SSA = 15 m^{2}kg^{-1}.

3.2. Temporal variations of T_s

Figure 7 shows the temporal variations of measured and simulated T_s over the northern and southern faces of the artificial snow mound. Simulation framework is detailed in Table 2.

Only the variations of T_s accounting for the viewing factor V are presented (step 5bis in Section 2.2.4).

The measured T_s of the southern face increases from -20.8°C at 06:00 UTC to reach a maximum at 12:00 of -0.9°C. Then, it decreases to fall at -21.8°C (22:00). The average mean T_s during the day is of -10.3°C for the southern face. The temperature of the northern face increases from -21.3°C (06:00) to -7.1°C (13:00) and then decreases to reach -23°C at 22:00. The average mean T_s during the day is of -14°C for the northern face. During the day, the difference in T_s between the two faces ranges from 0.5°C (06 :00) to 8.5°C (around 12:00), with an average of 3.8°C.

Simulated T_s is varies between -13.7°C (17:00) and -12.9°C (12:00) for the northern face and between -10.7°C (17:00) and -0.9°C (12:00) for the southern face. The average temperature during the day is -5°C for the southern facets and -13.2°C for the northern facets. During the day, the

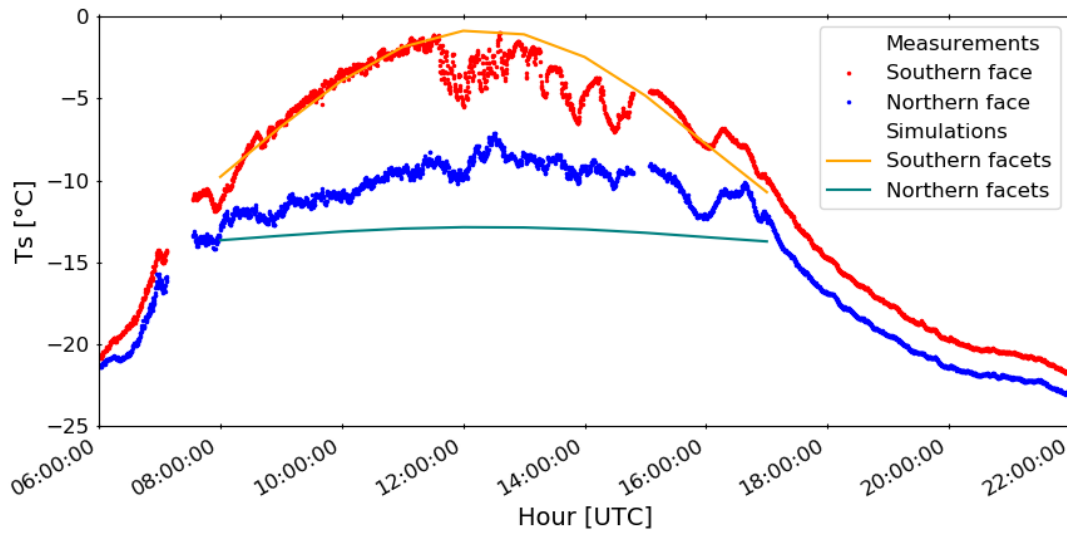difference in simulated T_s between the two faces varies from 3°C to 12°C, with an average of 8.2°C.

Figure 7: Temporal variations of measured T_s for southern and northern face (red and blue points, respectively) for March 26th, between 06:00 and 22:00 (UTC) and temporal variations of simulated T_s for southern and northern facets (orange and light blue lines, respectively) for March 26th, every hour between 08:00 and 17:00 (UTC). Simulations use an SSA = 30 $m^2 kg^{-1}$, $LW_d = 255$ Wm^{-2}, θ_s and φ_s ranging from 66° to 80° and 113°N to 252°N respectively to correspond to the hours of simulation.

The measured and simulated T_s show good agreement for the southern face of the mound (Figure 7). The simulation of T_s with the retrieval method developed in this study reproduces well the overall temporal variations throughout the day.

Nevertheless, between 12:00 and 16:00, short-time variations in measured T_s are visible, which are not reproduced by the simulations (see Figure 7). In the simulations, the atmospheric conditions were considered as clear-sky and LW_d was considered constant all along the day. LW_d was also taken from a weather station located outside of the measurement site (approximately 1 km away). These measured short-time variations are probably linked to a change in the local LW_d, which is sensitive to wind and clouds, and which can vary during the day. Similarly as for the southern face, the short-time variations throughout the day in measured T_s on the northern face are not reproduced by the simulations.

On the northern face, the simulated T_s constantly underestimates the measured T_s (see Figure 7). A possible explanation for this offset is discussed in Section 4.2.

The simulations performed for the Sodankylä experiment shows some promising results, by reproducing well the overall temporal evolution of T_s on the southern face of the mound. However, with the performed simulations, the evolution of simulated T_s on the northern face of the mound is always cooler than what was measured in the field. The turbulent fluxes were not taken into account in this study, and even though the wind was low, some heat is stil exchanged between the

surface and the atmoshere. This could explain the observed offset between simulations and measurements.

The method is further used to evaluate its capacity to reproduce spatial variations of T_s measured in a topographic rough terrain.

3.3. Spatial variations of T_s

The experiment at Col du Lautaret was designed to simulate the spatial variations of T_s on a topographic rough surface, and to evaluate the quality of the simulated T_s with field measurements. Simulation framework is detailed in Table 2. The simulations resulted in simulated T_s maps of the experiment sites. Only the simulated T_s map from the 09:00 simulation is presented here, the maps corresponding to the 11:00 and 13:00 simulations can be found in Appendix 2. Only the variations of T_s accounting for the viewing factor V are presented (step 5bis in Section 2.2.4).

Figure 8 shows a large range of simulated T_s, ranging between -11.5°C and 0°C over the whole area. The cold areas correspond to the northern faces of the area. Simulated T_s varies according to the topography of the terrain at the Col du Lautaret site.

The illumination conditions at 09:00 correspond to a sunlight coming from the South-East. A large part of the area is shadowed from sunlight (North facing sides of mountains, dark blue areas on the map), due to the illumination conditions: a sun illuminating the scene from the South-East at a large zenith angle (74°). We observe a constant temperature in these northern faces since they did not receive direct illumination yet.

T_s variations are more pronounced over South facing sides of the mountains. Southern faces teamperature depends on the amount of SW_d they receive, as shown in the Chamrousse experiment (Section 3.1). The quantity of SW_d received by a side depends of its exposition according to the sun position, and to its slope. For instance, the warmest area of Figure 8 is a South-East facing side, with a high slope (see level lines). The South facing sides re-illuminate the North facing sides and contribute to their warming. The shadowing of the site from the mountains is well visible on the map (dark blue areas), with a T_s of -11.5°C.

The maximum difference of simulated T_s is of 11°C at 11:00 and 10°C at 13:00. The maximum difference in simulated T_s decreases during the day, due to the warming of the snowpack throughout the day. Nevertheless, the maximum difference is still large because some areas of the site stay in the shadow no matter the hour, and are kept cool even though the illuminated areas reach 0°C.
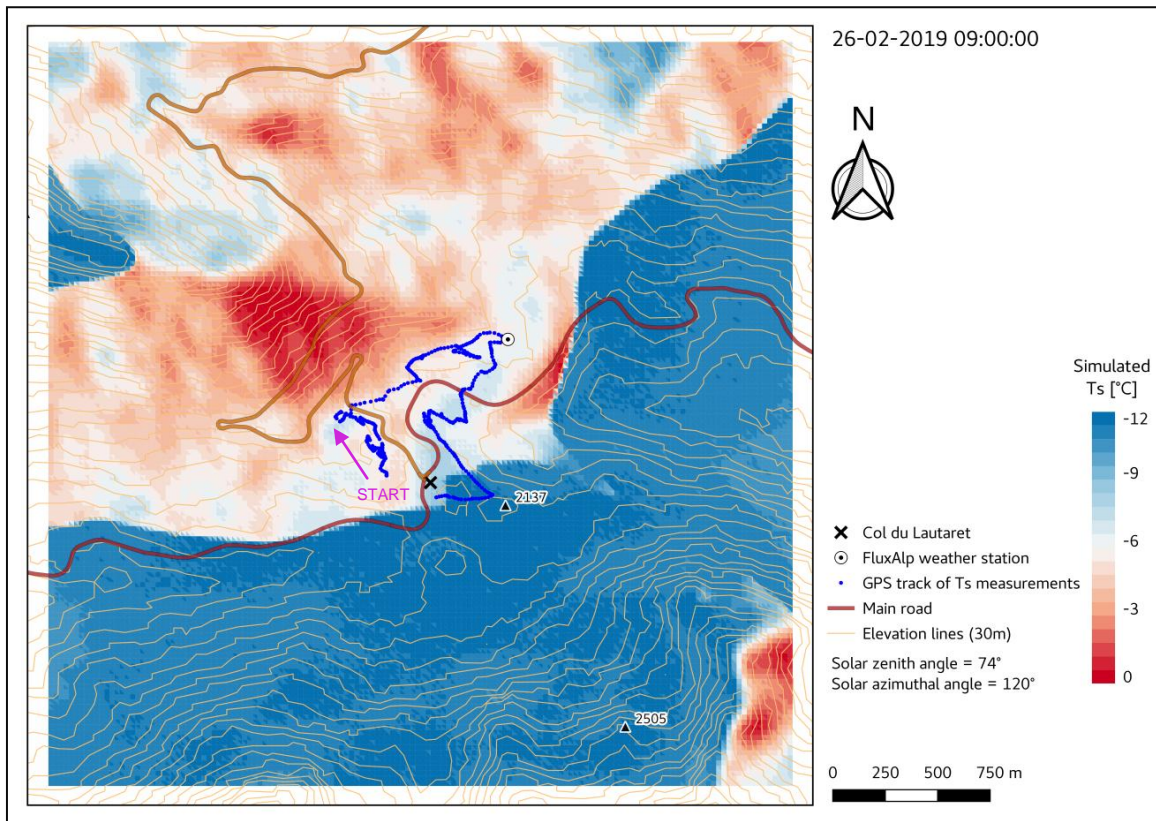
Figure 8: Spatial variations of simulated T_s at the Col du Lautaret site, February 26th, at 09:00 UTC ($\theta_s = 74°$ and $\varphi_s = 120°N$). The simulation was performed with an SSA = 15 $m^2 kg^{-1}$ and a $LW_d = 265$ Wm^{-2}. The transect of T_s measurements is shown in blue. The pink arrow represents the direction of the measurements from the starting point. The elevation lines are speced with 30 m. The closer they are, the steeper the slope is.

To evaluate the accuracy of the simulated T_s at a topographic scale, simulations are compared to measured T_s along the blue transect (shown in Figure 8).

T_s are extracted on the transect from the three simulated T_s maps (at 09:00, 11:00 and 13:00). Figure 9 shows the spatial variations of measured and simulated T_s along the transect (distance represented by the position index on the transect, 0 is the starting point, direction from starting point indicated by pink arrow in Figure 8). The time associated with the position of the measurements along the transect is shown in Figure 9 by the vertical grey dotted lines.

Along the transect, the measured T_s varies from -6.1°C to +1.3°C. Large variations in measured T_s occur on a small distance at the beginning of the transect. In the middle of the transect (position index between 200 and 500), the measured T_s is close to 0°C. At the beginning of the day, T_s variations are high since the low sun on the snow horizon allows the greatest variations of the radiative balance.

The associated simulated T_s are shown in Figure 9 for 09:00, 11:00 and 13:00 (full lines). Simulated T_s show spatial variations along the transect, ranging from: -11.4°C to -4.6°C for simulation at 09:00, -3.9°C to 0°C for simulation at 11:00 and -2.8°C to 0°C for simulation at 13:00.

If the minimum and maximum of measured T_s is respected, simulated T_s do not fit very well the measured T_s. The simulation at 09:00 do not reproduce the small-scale spatial variations of T_s at the corresponding time (i.e. beginning of transect, position index between 0 and 200). The similar observation can be made with the simulation at 13:00 (end of the transect). The 11:00 simulation is able to reproduce the melting-state of the snowpack in the middle part of the transect, but this is not a strong constraint for the validation.

The resolution of the mesh being of 30 m (resolution of the DEM used to run RSRT), the simulations reproduce the topographic variations of T_s at this scale. Measurements were taken on reliefs of about 30 m high and acquired each 10 m, so all the measured T_s variations can not be catch by the simulations due to the relatively low resolution of the mesh. In addition, we assume a constant SSA for the simulations whereas our measurements show variations likely caused by the metamorphism of snow grains due to the different temperature of the snowpack. These potential sources of uncertainties are further discussed in Section 4.3.
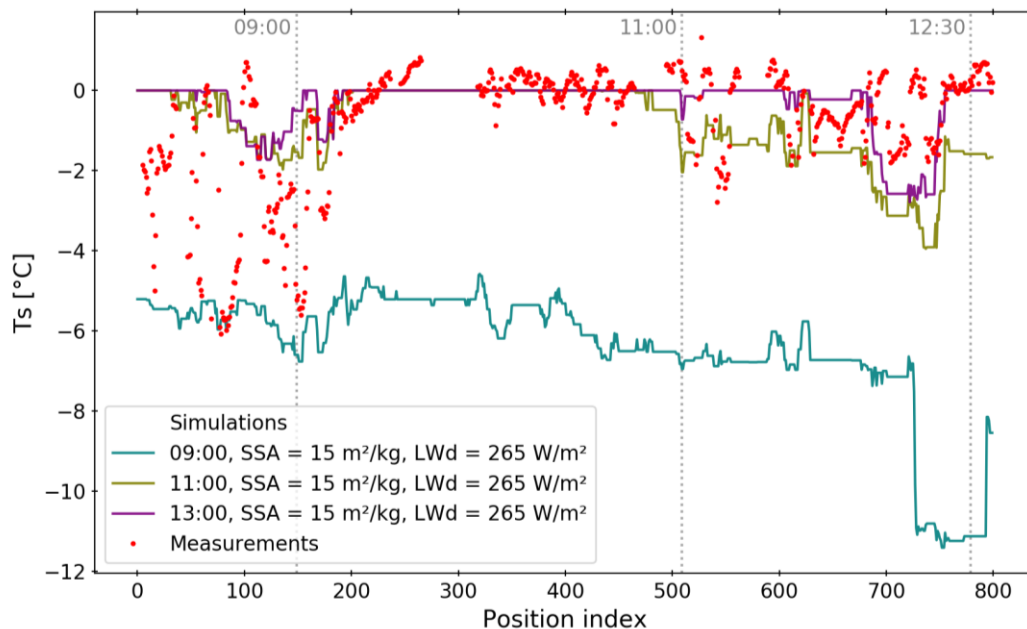

Figure 9: Spatial variations of measured (in red) and simulated (full lines) T_s along the transect at the Col du Lautaret site (see Figure 8). The position index represents the position on the transect. The measurement time associated with the position on the transect is represented by the vertical grey dotted lines. The measurements were taken on February 26th from 08:12 to 12:36 every 20 second with two IR120 probes. Simulations were performed at 09:00 (blue), 11:00 (green) and 13:00 (purple), with an SSA = 15 m²kg[-1] and $LW_d = 265\ Wm^{-2}$.

The experiment conducted at the Col du Lautaret site shows high spatial variations of measured T_s in mountainous areas (~ 6°C difference between a northern and a southern face). The model is

able to reproduce a pattern of T_s in mountain areas, but need to be run on a higher resolution mesh to be able to catch the T_s variations on small reliefs.

4. DISCUSSION

The evaluation of the RSRT model to simulate temporal and spatial variations of T_s have shown some promising results. Several points are discussed here to understand the potential sources of bias in this study for the measurements of T_s (Section 4.1), the temporal T_s simulations (Section 4.2) and the spatial T_s simulations (Section 4.3). Section 4.4 discusses the assumptions made to simulate T_s.

4.1. T_s measurements

The field measurements present some uncertainties that could contribute to the offset found between the simulated and measured T_s.

For the experiment at the Col du Lautaret site, measured T_s sometimes were above 0°C, which is not physically possible for a snow surface. This problem has two potential explanations.

The first one is the measurement protocole. The IR120 probes were fixed to a bar held by a backpack (see Figure 5). While moving along the transect, it is possible that probes were receiving some longwave radiation from snow-free surfaces (e.g. soil patches, skis, poles, etc.), and not only from the snow surface. This could have led to a warmer T_s than the actual T_s of the snow surface.

A second explanation lies in the uncertainty of the instrument, which is in principle 0.2°C but could be more when the instrument is subject to incoming and reflected solar radiation as it is the case on a snow surface.

4.2. Temporal variations of T_s

The results of the experiment at the Sodankylä site show: 1) an underestimation of simulated T_s compared to measured T_s on the northern face of the snow mound, and 2) the low performance of the simulations to reproduce short-time variations in measured T_s on both sides of the snow mound.

These differences between the simulated and measured T_s could be explained by the use of a constant LW_d in simulations. LW_d is a radiation flux from the atmosphere towards the surface, and mainly depends on the cloud and wind conditions. In our simulations, LW_d was considered equal to 255 Wm^{-2}, while the LW_d measured at the weather station indicated values varying from 200 to 271 Wm^{-2} during March 26th (see Table 2). In addition, some passing clouds and wind gusts were noticed in the field during that day.

To evaluate if these LW_d variations could explain the short-time variations in measured T_s not reproduced by our initial simulation, new T_s were simulated by using LW_d measured hourly instead of a constant LW_d (in step 4, section 2.2.4). Figure 10 shows the new simulated T_s and measured T_s at the Sodankyla site.
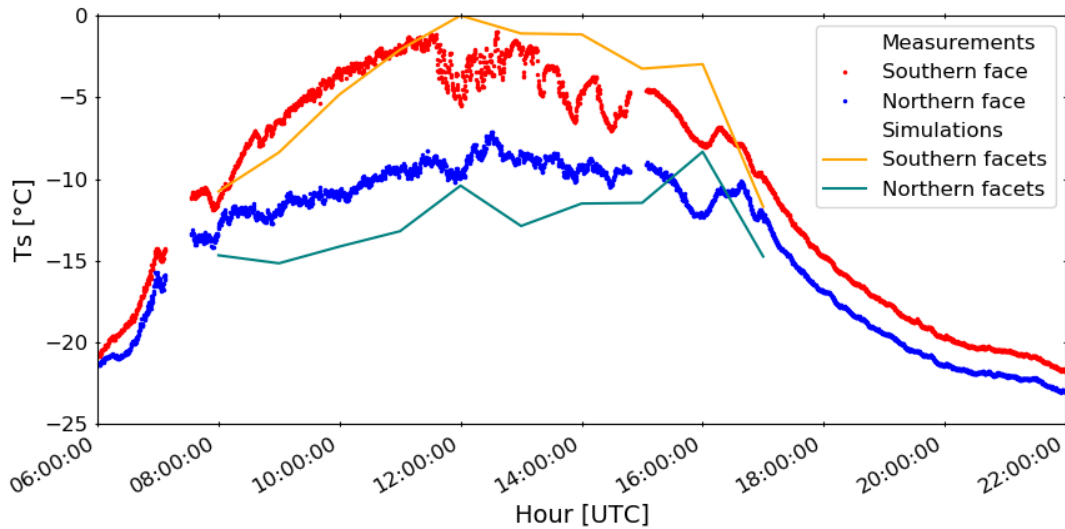

Figure 10: Same as Figure 7, excepth that the simulations were performed with a varying LW_d from 213 to 241 Wm^{-2}. The LW_d value used for each simulation hour corresponds to the measurement of LW_d at the weather station for the same hour.

Compared to Figure 7, Figure 10 shows that taking into account the variations of LW_d during the day allows us to reproduce some of the temporal variations of measured T_s on both sides of the snow mound.

Nevertheless, some of the variations in measured T_s is still not reproduced by the simulations. A possible explanation is the temporal resolution of simulations. One simulation per hour was performed between 08:00 and 17:00, whereas T_s was measured with a temporal resolution of 20 seconds. The time between two simulations was too long to be able to reproduce the short-time temporal variations of measured T_s. Yet another explanation is possible for the differences observed between the simulations and the measurements, that is the other heat fluxes in the energy budget that we assumed null. This issue is further discussed in Section 4.4.

4.3. Spatial variations of T_s

The results of the experiment at the Col du Lautaret site have shown a relatively poor agreement between simulated and measured T_s along the transect.

A first explanation for this poor agreement has been mentioned in Section 3.3: a low spatial resolution of the mesh used to simulate T_s compared to high spatial resolution of measurements. Indeed, the spatial resolution of the simulations are 30 m while the measurements were acquired with a resolution of 10 m, so that simulations can not reproduce the variations captured by the

23

measurements. A way to improve simulations would be to construct a 3D mesh from a DEM with a higher resolution. In addition, the DEM used to produce the 3D mesh for simulations was acquired in the summertime when the terrain was free of snow. The topography of the terrain and the slopes in the wintertime can be smoothed compared to snow-free conditions.

Another possible explanation for the observed differences between simulated and measured T_s is the use of a constant value of SSA in simulations (15 m^2kg^{-1}) considered constant during the day and over the entire mesh. However, SSA measurements acquired in the field showed high spatial variations along the transect, with values varying from 5 to 30 m^2kg^{-1}, with SSA values from 5 to 10 m^2kg^{-1} for southern faces, 15 – 30 m^2kg^{-1} for northern faces, and around 5 m^2kg^{-1} for the bottom of the cavities. When SSA decreases, snow albedo decreases in the near-infrared (Warren et al., 1998) and the absorbed radiation increases, leading to a warming of the surface. This T_s sensitivity to the SSA is shown in Figure 11. When SSA decreases from 30 to 15 m^2kg^{-1}, the average simulated T_s along the transect becomes 3°C warmer; when SSA decreases from 15 to 5 m^2kg^{-1}, the average simulated T_s along the transect becomes 6°C warmer. These results obtained with uniform SSA over the whole area illustrates the need to refine the simulations with varying SSA at least along the transect where SSA were measured in the field.
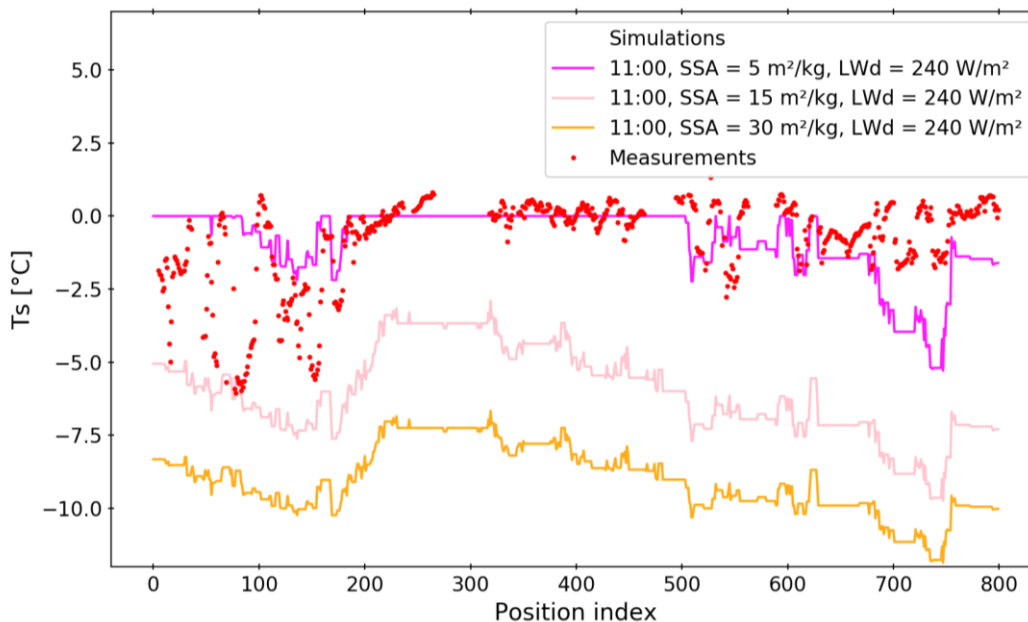

Figure 11: Same as Figure 9, except that the simulations were performed with an SSA of 5 m^2kg^{-1} (fuschia), 15 m^2kg^{-1} (pink) and 30 m^2kg^{-1} (orange).

4.4. Energy budget

All of the T_s simulations performed in this study were based on several assumptions.
The study focused on the radiative component R_{net} of the energy budget only, considering H, L and G from equation [1] equal to zero. This assumption was based on the filed conditions, that were considered stable, with no wind, rain or any phenomena that could cause additional heat fluxes at

the surface. Nevertheless, in reality, these heat fluxes may not have been negligible and contributed to cool or warm the surface. At Sodankylä, there were some wind gusts during the day that could have influenced the energy budget of the studied surface. The estimated heat fluxes L and H by the FMI were varying during the day between -4 and 6 Wm^{-2} for the latent heat flux (L) and between -8 to 212 Wm^{-2} for the sensible heat flux (H).

The data from the FluxAlp station (Col du Lautaret) also show some variations of the wind (up to 5 ms^{-1} during that day).

The snowpack inertia was also neglected: the energy flux lost away in the underlying layers of the snowpack was considered null. This assumption was also made based on the field conditions: the snowpack was considered in equilibrium with the atmophere when measurements were conducted. However, this assumption could lead to a bias in the radiative balance simulations, especially in early hours when the sunlight just hit the surface and the snowpack starts to warm.

In the simulation of the radative balance of the facets, the attenuation of the intensity of the photon along its path is only due to the absorption by the surface when the photon collides with the surface. In reality, a second process attenuates the intensity of a photon before it hits the surface, that is the atmopshere attenuation. The energy of each photon is attenuated when it goes through the atmopshere, and this attenuation depends on the atmopshere composition (concentration of aerosol, ozone, etc.). This phenomena was not accounted for in our simulations. Nevertheless, accouting for this effect would have increase the accuracy of our simulations, especially for simulations at a large scale (Col du Lautaret). A future work would be to compare simulated T_s maps with thermal infrared satellite observations, and this effect should be taken into account.

5. SUMMARY AND CONCLUSION

This study proposes a method to compute the snow surface temperature based on the outputs of three different models (SBDART, ART and RSRT) over different rough surfaces and at different scales (meter-scale to topographic).

The method was first tested on an artificial rough surface at Chamrousse, in the French Alps. Simulations were performed on this surface and show a warming in the cavities of the rough surface due to multiple reflection, trapping effect of photons and re-illumination from warm facets. These results are coherent with previous studies (Kuchiki et al., 2011, Lhermitte et al., 2014). The method is able to reproduce the increased absorption in the cavities of the roughness features as well as the trapping effect of the photons.

The method was further applied to estimate temporal variations of T_s on a meter-scale artificial rough surface (snow mound) at the Sodankylä experiment site. Results of this experiment show good agreement on the overall temporal variations of simulated an measured T_s on the southern face of the snow mound. The difference in measured T_s between the two faces during the day was

minimum when the Sun was not up (0.5°C at 06:00) and maximum (8.5°C) at 12:00. The difference in simulated T_s between the two faces during the day was minimum at 08:00 (3°C) and maximum (12°C) at 12:00.

Results show an offset between simulations and measurements at a short-time temporal resolution. This highlights the need to perform simulations at a finer temporal resolution to be able to catch these variations.

Lastly, the method was used to produce simulated T_s maps in a mountainous area at the Col du Lautaret (French Alps). Spatial simulations were compared with T_s measurements acquired over a large transect. Results of this experiment show a difference in T_s between the northern and southern faces is about ~ 6°C. Simulated T_s do not reproduce the spatial variations of measured T_s at a low scale, probaby due to the difference in spatial resolution between simulations and measurements.

This study highlights the need to perform simulations at a finer temporal scale and at a finer spatial scale to be able to reproduce the short-time and very local variations in the surface temperature. Generally, this study show promising results in simulating the snow T_s of a rough surface at different scales. The method used to simulate T_s would need further development in order to improve simulations.

References

Adams, E. E., Slaughter, A. E., McKittrick, L. and Miller, D. A.: Local terrain-topography and thermal-properties influence on energy and mass balance of a snow cover, Ann. Glaciol., 52(58), 169–175, doi:10.3189/172756411797252257, 2011.

Ambach, W.: The Influence of Cloudiness on The Net Radiation Balance of A Snow Surface with High Albedo, J. Glaciol., 13(67), 73–84, doi:10.1017/s0022143000023388, 1974.

Aoki, T., Aoki, T., Fukabori, M. and Uchiyama, A.: Numerical Simulation of the Atmospheric Effects on Snow Albedo with a Multiple Scattering Radiative Transfer Model for the Atmosphere-Snow System, J. Meteorol. Soc. Japan. Ser. II, 77(2), 595–614, doi:10.2151/jmsj1965.77.2_595, 1999.

Aoki, T., Motoyoshi, H., Kodama, Y., Yasunari, T. J. and Sugiura, K.: Variations of the snow physical parameters and their effects on albedo in Sapporo, Japan, Ann. Glaciol., 46(1994), 375–381, doi:10.3189/172756407782871747, 2007.

Armstrong, R. L. and Brun, E.: Snow and Climate: Physical Processes, Surface Energy Exchange and Modeling, edited by Cambridge University Press., 2008.

Arnaud, L., Picard, G., Champollion, N., Domine, F., Gallet, J. C., Lefebvre, E., Fily, M. and Barnola, J. M.: Measurement of vertical profiles of snow specific surface area with a 1cm resolution using infrared reflectance: instrument description and validation, J. Glaciol., 57(201), 17–29, doi:10.3189/002214311795306664, 2011.

Barry, R. G.: The Role of Snow and Ice in the Global Climate System: A Review, Polar Geogr., 26(3), 235–246, doi:10.1080/789610195, 2002.

Van den Broeke, M., Reijmer, C. and Van de Wal, R.: Surface radiation balance in Antarctica as measured with automatic weather stations, J. Geophys. Res., 109, doi:10.1029/2003JD004394, 2004.

Van den Broeke, M., Van As, D., Reijmer, C. and Van de Wal, R.: Sensible heat exchange at the Antarctic snow surface: A study with automatic weather stations, Int. J. Climatol., 25(8), 1081–1101, doi:10.1002/joc.1152, 2005.

Brun, E., Martin, E., Simon, V., Gendre, C. and Coleou, C.: An energy and mass model of snow cover suitable for operational avalanche forecasting, J. 0/Glaciology, 35(12), 1, 1989.

Brun, E., David, P., Sudul, M. and Brunot, G.: A numerical model to simulate snow-cover stratigraphy for operational avalanche forecasting, J. Glaciol., 38(128), 13–22, 1992.

Brun, E., Six, D., Picard, G., Vionnet, V., Arnaud, L., Bazile, E., Boone, A., Bouchard, A., Genthon, C., Guidard, V., Le Moigne, P., Rabier, F. and Seity, Y.: Snow/atmosphere coupled simulation at Dome C, Antarctica, J. Glaciol., 57(204), 721–736, doi:10.3189/002214311797409794, 2011.

Brun, É., Vionnet, V., Morin, S., Boone, A., Martin, É., Faroux, S., Le Moigne, P. and Willemet, J.-M.: Le modèle de manteau neigeux Crocus et ses applications, La Météorologie, 2012.

Carmagnola, C. M., Domine, F., Dumont, M., Wright, P., Strellis, B., Bergin, M., Dibb, J., Picard, G., Libois, Q., Arnaud, L. and Morin, S.: Snow spectral albedo at Summit, Greenland: Measurements and numerical simulations based on physical and chemical properties of the snowpack, Cryosphere, 7(4), 1139–1160, doi:10.5194/tc-7-1139-2013, 2013.

Carroll, J. J. and Fitch, B. W.: Effects of solar elevation and cloudiness on snow albedo at the South Pole, J.

Geophys. Res. Ocean., 86(C6), 5271–5276, doi:10.1029/JC086iC06p05271, 1981.

Dozier, J.: A clear-sky spectral solar radiation model for snow- covered mountainous terrain, Water Resour. Res., 16(4), 709–718, doi:10.1029/WR016i004p00709, 1980.

Dubayah, R., Dozier, J. and Davis, F.: The distribution of clear-sky radiation over varying terrain, 12th Can. Symp. Remote Sens. Geosci. Remote Sens. Symp., 2, 885–888, doi:10.1109/IGARSS.1989.579024, 1989.

Dumont, M., Brissaud, O., Picard, G., Schmitt, B., Gallet, J. C. and Arnaud, Y.: High-accuracy measurements of snow Bidirectional Reflectance Distribution Function at visible and NIR wavelengths - comparison with modelling results, Atmos. Chem. Phys., 10(5), 2507–2520, doi:10.5194/acp-10-2507-2010, 2010.

Dumont, M., Sirguey, P., Arnaud, Y. and Six, D.: Monitoring spatial and temporal variations of surface albedo on Saint Sorlin Glacier (French Alps) using terrestrial photography, Cryosph., 5(3), 759–771, doi:10.5194/tc-5-759-2011, 2011.

Dumont, M., Arnaud, L., Picard, G., Libois, Q., Lejeune, Y., Nabat, P., Voisin, D. and Morin, S.: In situ continuous visible and near-infrared spectroscopy of an alpine snowpack, Cryosphere, 11(3), 1091–1110, doi:10.5194/tc-11-1091-2017, 2017.

Etchevers, P., Martin, E., Brown, R., Fierz, C., Lejeune, Y., Bazile, E., Boone, A., Dai, Y.-J., Essery, R. and Fernandez, A.: Validation of the energy budget of an alpine snowpack simulated by several snow models (Snow MIP project), Ann. Glaciol., 38, 150–158, 2004.

Gallet, J. C., Domine, F., Arnaud, L., Picard, G. and Savarino, J.: Vertical profile of the specific surface area and density of the snow at Dome C and on a transect to Dumont D'Urville, Antarctica - Albedo calculations and comparison to remote sensing products, Cryosphere, 5(3), 631–649, doi:10.5194/tc-5-631-2011, 2011.

Jamieson, B. and Schirmer, M.: Measuring Snow Surface Temperature : why, why not and how ?, in Proceedings of the 2016 International Snow Science Workshop., 2016.

Kiehl, J. T. and Trenberth, K. E.: Earth's annual global mean energy budget, Bull. Am. Meteorol. Soc., 78(2), 197–208, 1997.

Kokhanovsky, A. A. and Zege, E. P.: Scattering optics of snow., Appl. Opt., 43(7), 1589–1602, doi:10.1364/AO.43.001589, 2004.

Kuchiki, K., Aoki, T., Niwano, M., Motoyoshi, H. and Iwabuchi, H.: Effect of sastrugi on snow bidirectional reflectance and its application to MODIS data, J. Geophys. Res. Atmos., 116(18), 1–15, doi:10.1029/2011JD016070, 2011.

Laurent, J. P., Cohard, J. M., Biron, R., Delbart, F., Aubert, S. and Choler, P.: «FLUXALP »: Un projet de développement d'une station de mesures éco-climatiques au Col du Lautaret, Hautes-Alpes, France., 2014.

Larue, F., Picard, G., Arnaud, L., Ollivier, I., Delcourt, C., Lamare, M., Revuelto, J., Dumont, M.: Albedo sensitivity over macroscopic rough surfaces using a new ray tracing model, in preparation.

Lee, W., Liou, K., Wang, C., Gu, Y., Hsu, H. and Li, J. F.: Impact of 3D Radiation Topography Interactions on Surface Temperature and Energy Budget Over the Tibetan Plateau in Winter, J. Geophys. Res. Atmos., 124(3), 1537–1549, doi:10.1029/2018JD029592, 2019.

Lhermitte, S., Abermann, J. and Kinnard, C.: Albedo over rough snow and ice surfaces, Cryosphere, 8(3), 1069–1086, doi:10.5194/tc-8-1069-2014, 2014.

Li, J. F., Lee, W., Yu, J., Hulley, G., Fetzer, E., Chen, Y. and Wang, Y.: The impacts of precipitating

hydrometeors radiative effects on land surface temperature in contemporary GCMs using satellite observations, J. Geophys. Res. Atmos., 121, 67–79, doi:10.1002/2015JD023776, 2016.

Libois, Q., Picard, G., Dumont, M., Arnaud, L., Sergent, C., Pougatch, E., Sudul, M. and Vial, D.: Experimental determination of the absorption enhancement parameter of snow, J. Glaciol., 60(222), 714–724, doi:10.3189/2014j0g14j015, 2014.

Lucht, W., Hyman, A. H., Strahler, A. H., Barnsley, M. J., Hobson, P. and Muller, J. P.: A comparison of satellite-derived spectral albedos to ground-based broadband albedo measurements modeled to satellite spatial scale for a semidesert landscape, Remote Sens. Environ., 74(1), 85–98, doi:10.1016/S0034-4257(00)00125-5, 2000.

Male, D. H. and Granger, R. J.: Snow surface energy exchange, Water Resour. Res., 17(3), 609–627, doi:10.1029/WR017i003p00609, 1981.

Picard, G., Libois, Q., Arnaud, L., Verin, G. and Dumont, M.: Development and calibration of an automatic spectral albedometer to estimate near-surface snow SSA time series, Cryosphere, 10(3), 1297–1316, doi:10.5194/tc-10-1297-2016, 2016.

Plüss, C. and Ohmura, A.: Longwave radiation on snow-covered mountainous surfaces, J. Appl. Meteorol., 36(6), 818–824, 1997.

Pomeroy, J. W., Essery, R. L. H. and Helgason, W. D.: Aerodynamic and Radiative Controls on the Snow Surface Temperature, J. Hydrometeorol., 17(8), 2175–2189, doi:10.1175/jhm-d-15-0226.1, 2016.

Raleigh, M. S., Landry, C. C., Hayashi, M., Quinton, W. L. and Lundquist, J. D.: Approximating snow surface temperature from standard temperature and humidity data: New possibilities for snow model and remote sensing evaluation, Water Resour. Res., 49(12), 8053–8069, doi:10.1002/2013WR013958, 2013.

Ricchiazzi, P., Yang, S. and Gautier, C.: SBDART: A Practical Tool for Plane-Parallel Radiative Transfer in the Earth's Atmosphere, 1996.

Ricchiazzi, P., Yang, S., Gautier, C. and Sowle, D.: SB DART: A Research and Teaching Software Tool for Plane-Parallel Radiative Transfer in the Earth's Atmosphere, Bull. Am. Meteorol. Soc., 79(10), 2101–2114, 1998.

Shea, C. and Jamieson, B.: Some fundamentals of handheld snow surface thermography, Cryosphere, 5(1), 55–66, doi:10.5194/tc-5-55-2011, 2011.

Tuzet, F., Dumont, M., Lafaysse, M., Picard, G., Arnaud, L., Voisin, D., Lejeune, Y., Charrois, L., Nabat, P. and Morin, S.: A multilayer physically based snowpack model simulating direct and indirect radiative impacts of light-absorbing impurities in snow, Cryosphere, 11(6), 2633–2653, doi:10.5194/tc-11-2633-2017, 2017.

Vavrus, S.: The role of terrestrial snow cover in the climate system, Clim. Dyn., 29(1), 73–88, doi:10.1007/s00382-007-0226-0, 2007.

Vionnet, V., Brun, E., Morin, S., Boone, A., Faroux, S., Le Moigne, P., Martin, E. and Willemet, J. M.: The detailed snowpack scheme Crocus and its implementation in SURFEX v7.2, Geosci. Model Dev., 5(3), 773–791, doi:10.5194/gmd-5-773-2012, 2012.

Wang, W., Zender, C. S., Van As, D., Smeets, P. C. J. P. and Van Den Broeke, M. R.: A Retrospective, Iterative, Geometry-Based (RIGB) tilt-correction method for radiation observed by automatic weather stations on snow-covered surfaces: Application to Greenland, Cryosphere, 10(2), 727–741, doi:10.5194/tc-10-727-2016, 2016.

Warren, S. G.: Optical properties of snow, Rev. Geophys. Sp. Phys., 20(1), 67–89, doi:10.1029/RG020i001p00067, 1982.

Warren, S. G. and Wiscombe, W. J.: A Model for the Spectral Albedo of Snow. II: Snow Containing Atmospheric Aerosols, J. Atmos. Sci., 37(12), 2734–2745, 1980.

Warren, S. G., Brandt, R. E. and O'Rawe Hinton, P.: Effect of surface roughness on bidirectional reflectance of Antarctic snow, J. Geophys. Res. Planets, 103(E11), 25789–25807, doi:10.1029/98JE01898, 1998.

Weller, G.: The Heat and Mass Balance of Snow Dunes on the Central Antarctic Plateau, J. Glaciol., 8(53), 277–284, doi:10.3189/S0022143000031257, 1969.

Wiscombe, W. J. and Warren, S. G.: A model for the spectral albedo of snow. I: Pure snow, J. Atmos. Sci., 37(12), 2712–2733, 1980.

Web 1: Campbell Scientific, IR120 – Radiometer - Infrared Remote Temperature Sensors, viewed May 29th 2019, https://www.campbellsci.eu/ir120.

Web 2: Campbell Scientific, PT100/3, viewed May 29th 2019, https://www.campbellsci.eu/pt100-3.

Web 3: Observations at the Arctic Space Center, Finnish Meteorological Institute, Sodankylä, viewed April 9th, http://litdb.fmi.fi/.

Web 4: NASA EarthData, viewed Februrary 20th 2019, https://search.earthdata.nasa.gov/search?q=DEM&ok=DEM.

Appendix

Appendix 1: Flow chart of a photon path in the RSRT model. $\vec{\imath}$ is the incident direction of the photon, $\overrightarrow{\imath_{z,p}}$ is the z axis component of the photon at the end of its path (Larue et al., in prep.).
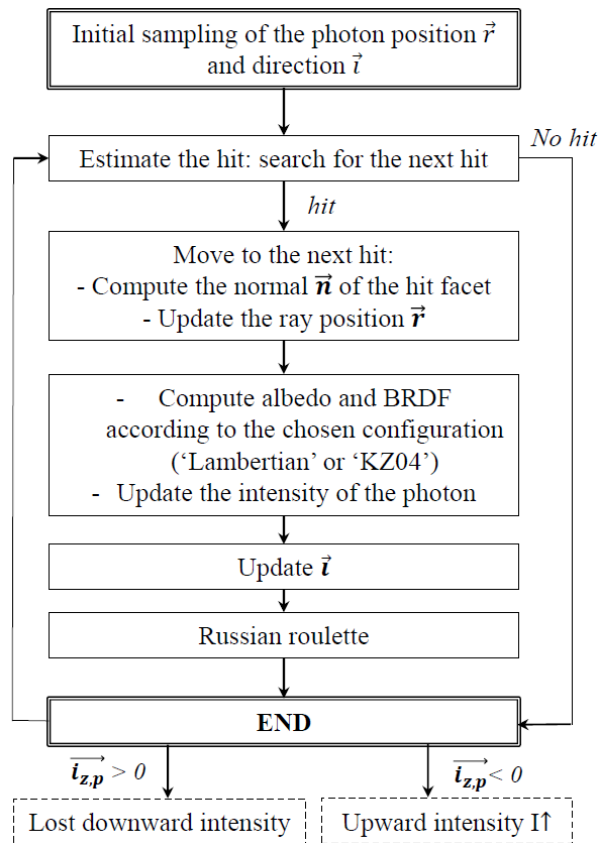
Appendix 2: Simulated T_s maps for the 11:00 (a) and 13:00 (b) simulations at the Col du Lautaret site.

26-02-2019 13:00:00

b

N

Simulated
Ts [°C]

−12

−9

−6

−3

0

× Col du Lautaret
⊙ FluxAlp weather station
• GPS track of Ts measurements
— Main road
   Elevation lines (30m)

Solar zenith angle = 54°
Solar azimuthal angle = 184°

2137

2505

0   250   500   750 m